RESEARCH PAPER

Bioactive Rutin@Hydroxyapatite-Halloysite nanocomposites: synergistic antibacterial and osteogenic effects for bone tissue regeneration

***Jayasudha Paramanithi*[1], *Balakrishnan Munisamy*[1], *Bhalaji Pudupettai Rajagopal*[1*]**

[1] *Department of Chemistry, Government Arts College for Men, Krishnagiri, Tamil Nadu, India*

ABSTRACT

The present study describes the synthesis, characterization, and *in vitro* biological effectiveness of a new Rutin@Hydroxyapatite-Halloysite (Ru@HA-HNT) nanocomposite for the treatment of osteomyelitis and the regeneration of bone tissue. FT-IR and XRD measurements validated the successful incorporation of rutin (Ru) without structural modification, whereas TEM and SEM demonstrated a consistent coating of spherical Hydroxyapatite (HA) particles on tubular HNTs, offering a significant surface area for Ru adsorption. Biological evaluations utilizing MC3T3-E1 pre-osteoblast cells indicated that the nanocomposite markedly improved biocompatibility and promoted proliferation of cells. The material's capacity to reduce reactive oxygen species (ROS) levels and preserve mitochondrial membrane potential (MMP) further emphasized its antioxidant characteristics and cellular stability. The nanocomposite demonstrated significant antibacterial effectiveness against *Staphylococcus aureus (S.aureus)*, attaining a killing efficiency of 98.4% by day 14. Moreover, osteogenic assays demonstrated a significant enhancement in differentiation; by day 14, the Ru@HA-HNT group displayed ALP activity and calcium mineralization (ARS) levels that were 19% and 16% superior to the controls, respectively. Immunofluorescence studies verified the elevation of critical osteogenic markers (RUNX2, ALP, COL I, and OCN), substantiating the material's function in promoting bone formation. The findings indicate that the Ru@HA-HNT nanocomposite is an effective, multifunctional material for concurrently addressing osteomyelitis and facilitating bone tissue regeneration.

Keywords: *Osteomyelitis, Bone regeneration, Nanocomposites, Antibacterial Agents, Signal Transduction*

How to cite this article

Paramanithi J, Munisamy B, Pudupettai Rajagopal Bh. Bioactive Rutin@Hydroxyapatite-Halloysite nanocomposites: synergistic antibacterial and osteogenic effects for bone tissue regeneration. Nanomed J. 2026; 13: 1-. doi: 10.22038/nmj.2026.92717.2347

INTRODUCTION

Osteomyelitis, a severe inflammatory infection of the bone and bone marrow, presents a continuous and considerable problem in orthopedic surgery. The illness is mostly attributed to bacterial infections, with *S. aureus* identified as the principal etiological agent in both acute and chronic stages. The treatment of bone infections is particularly difficult due to the unique physiological characteristics of bone tissue; specifically, the avascular nature of necrotic bone matrix and sequestra severely restricts the efficient penetration of systemic medications to the infection site [1, 2]. Surgical debridement to excise necrotic bone and contaminated tissue is fundamental to osteomyelitis management; yet, it frequently leads to substantial bone abnormalities necessitating intricate reconstructive interventions [3,4]. Moreover, issues including patient non-adherence frequently impair the efficacy of systemic treatments, thereby increasing the emergence of Multidrug-Resistant (MDR) infections. These limitations highlight a significant therapeutic need for “dual-function biomaterials” that can provide localized antibacterial effects while also serving as a scaffold to restore skeletal integrity [5]. Nanomaterials offer a promising innovative strategy; they may be designed to mimic the natural architecture of bone, thus addressing infection while promoting cellular adhesion, proliferation, and healing [6,7].

Hydroxyapatite (HA, $Ca_{10}(PO_4)_6(OH)_2$)is widely regarded as a leading biomaterial for reconstruction owing to its close chemical resemblance to the inorganic phase of native human bone.Its superior biocompatibility, osteoconductivity, and structural resemblance to natural bone have established it as a fundamental material in bone tissue engineering and regenerative medicine for years. As an osteoconductive component, HA offers an appropriate scaffold that directs the proliferation of

* *Corresponding author(s):* Bhalaji Pudupettai Rajagopal, PhD, Professor, Department of Chemistry, Government Arts College for Men, Krishnagiri-635 001, Tamil Nadu, India. Phone: +97 87944334; Email: *prbhalaji@yahoo.in*.

Note. This manuscript was submitted on November 12, 2025; approved on February 03, 2026.

new bone tissue, facilitating the migration, adhesion, and proliferation of osteoblasts and other osteogenic cells on its surface [8,9]. Despite Hydroxyapatite (HA) exhibiting remarkable osteoconductivity and biocompatibility, its clinical utilization is significantly constrained by two primary limitations: inherent mechanical brittleness and an absence of antimicrobial properties. In situations susceptible to infection, pure HA scaffolds may inadvertently act as substrates for bacterial colonization, resulting in the failure of the bone regeneration process [10]. To tackle this issue, research has concentrated on functionalizing HA to display intrinsic antibacterial capabilities; nevertheless, traditional methods that depend on synthetic antibiotics are under growing scrutiny due to increasing resistance and cytotoxicity concerns. In addition to biological issues, the intrinsic fragility and diminished fracture toughness of HA undermine its structural integrity in load-bearing defects. To address these issues, Halloysite Nanotubes (HNTs) naturally occurring aluminosilicate clays have been utilized as a strategic reinforcing component. Unlike systems primarily designed for drug delivery, HNTs in the present composite system are incorporated predominantly as reinforcing nanofillers. Their incorporation significantly improves the mechanical strength and structural integrity of the scaffold for potential load-bearing applications, while their distinctive tubular structure offers a high-surface-area platform for advantageous cell-material interactions and the efficient loading of non-antibiotic antimicrobial agents [11–15].

The naturally occurring flavonoid Rutin (Ru, $C_{27}H_{30}O_{16}$) has garnered considerable interest in orthopedic tissue engineering owing to its diverse biological properties. Studies have demonstrated that Ru exhibits significant antioxidant, anti-inflammatory, and antibacterial activities [16-18]. In the context of osteomyelitis, its antioxidant properties neutralize harmful ROS produced by inflammation, while its antibacterial mechanism disrupts bacterial cell membranes and inhibits essential enzymes, rendering it effective against *S. aureus* [19, 20]. In addition to infection management, Ru serves as a potential osteogenic agent; recent research demonstrates its ability to increase mesenchymal stem cell differentiation, increase bone-related protein expression (such as alkaline phosphatase and osteocalcin), and stimulate matrix mineralization [21-23]. The clinical utility of free Ru is impeded by its low solubility in water and inadequate stability. This integration utilizes Ru to modify the scaffold surface, addressing its solubility constraints while providing sustained biological activity [24, 25]. However, a critical gap remains in the development of a ternary nanocomposite that synergistically integrates the mechanical reinforcement of HNTs with the osteoconductivity of HA and the biological efficacy of Ru, providing a dual-functional strategy that concurrently eliminates infection and promotes bone healing. Existing literature predominantly emphasizes binary (HA/HNT) composites aimed exclusively at mechanical enhancement [13], or, conversely, antibiotic-embedded scaffolds that exhibit burst release kinetics and exacerbate antimicrobial resistance [26]. We propose that the integration of both Ru and HNTs into the HA matrix will produce a dual-functional surface, with HNTs reinforcing structural integrity and Ru providing contact-mediated antibacterial efficacy against *S. aureus* [27]. This method seeks to inhibit initial bacterial adherence by directly disrupting the membrane, a mechanism specifically assessed in this study using fluorescence-based Live/Dead (AO/PI) analysis.

The novelty of this research is the development of a dual-functional Ru@HA-HNT nanocomposite: a bio-functionalized system aimed at concurrently eliminates infection and promotes bone healing without the need for conventional antibiotic loading. The main goal is to synthesize this nanocomposite and assess its physicochemical stability and mechanical performance for cancellous bone applications. The study aims to assess the antibacterial activity against *S. aureus* by measuring the colony-forming units and observing bacterial membrane rupture by fluorescence microscopy. The research additionally attempts to show the material's superior osteogenic capability, specifically its capacity to mitigate oxidative stress and improve the protein expression of essential differentiation markers (RUNX2, ALP, COL I, and OCN), thereby establishing Ru@HA-HNT as a comprehensive, infection-resistant scaffold for osteomyelitis therapy.

MATERIAL AND METHODS

Chemicals

Rutin, $Al_2Si_2O_5(OH)_4$, $Ca(NO_3)_2{\cdot}4H_2O$, and $(NH_4)_2HPO_4$ were purchased from Sigma Aldrich Chemicals. All reagents and chemicals were used in analytical grade without any further purification.

Synthesis of HA-HNT and Ru2@HA-HNT nanocomposite

The HA-HNT nanocomposites were made using an *in-situ* co-precipitation method. In summary, 0.5 g of HNTs was mixed in 50 mL of deionized (DI) water and subjected to ultrasonication for

25 min to achieve uniform dispersion. Independently, 0.59 g of $Ca(NO_3)_2{\cdot}4H_2O$ was dissolved in 20 mL of DI water and incorporated into the HNT dispersion while maintaining continuous agitation. A solution consisting of 0.20 g of $(NH_4)_2HPO_4$ was progressively added into 25 mL of DI water. The pH of the resultant suspension was altered to 10 using aqueous NH_3, and the mixture was sustained at 60°C for 10 hr to promote the nucleation of HA onto the HNT surface. The resultant product was obtained *via* centrifugation, meticulously washed with DI water, dried overnight at 60°C.

To fabricate the Ru@HA-HNT, 0.1 g of the prepared HA-HNT matrix was dispersed in ethanolic rutin solutions at concentrations of 1%, 2%, and 3% (w/v). The samples were labeled as Ru1@HA-HNT, Ru2@HA-HNT, and Ru3@HA-HNT, respectively. The suspensions were gently stirred at ambient temperature for 5 hr, followed by incubation at 37°C overnight to promote drug adsorption. The final products were obtained using centrifugation, washed with DI water to eliminate loosely bound rutin, and dried overnight at 60°C.

Characterization of prepared nanocomposites

The FT-IR spectra of nanocomposites were obtained using a Thermo FTIR (Nicolet iS50, Thermo Fisher Scientific Ltd., USA) within the range of 4000 cm^{-1} to 500 cm^{-1} to identify the surface functional groups of Ru2@HA-HNT. The XRD patterns were analyzed using an X-ray diffractometer (MiniFlex-600, Rigaku Co., Japan) with a scanning angle ranging from 5° to 80° at a scanning speed of 10°/min. The structural morphology of nanocomposites was examined using a Carl-Zeiss Field-Emission Scanning Electron Microscope (ZEISS, Gemini SEM 300). The nanostructure and aggregation of HA in HNT were examined using a high-resolution transmission electron microscope (HR-TEM) (FEI Tecnai G2 20 S-Twin). The nanostructure was diluted with ethanol and subsequently drop-cast (5 µL) onto the copper grid. They were subsequently recorded following the evaporation of the solvent. The mechanical properties of the nanocomposites were assessed utilizing a universal testing machine (Shimadzu with an Instron 5848 microtensile tester).

Cell culture

The murine calvarial osteoblast-like cell line (MC3T3-E1), purchased from the American Type Culture Collection (ATCC number: CRL-2593), was cultivated in a DMEM/F-12 nutrient mixture, augmented with 10% FBS and 1% penicillin and streptomycin. Cells were cultured in a humidified incubator at 37°C with 5% CO_2. MC3T3-E1Cells were allowed to proliferate until achieving 80% confluence. After achieving 80% confluence, the cells were then detached using 0.25% trypsin-EDTA.

Cell viability analysis

The viability of MC3T3-E1 cells was assessed with the MTT test at 1, 2, and 3 days following the stimulation of osteogenic differentiation. Cells were inoculated at a density of 6×10^3 cells per well in a 96-well plate and incubated for 24 hr in α-MEM at 37°C with 5% CO_2. After the introduction of fresh α-MEM, serially diluted Ru2@HA-HNT (10 to100 µg/mL) was administered to the cultures. Following 18 hr incubation, 15 µL of MTT solution was introduced to each well and incubated for an additional 4 hr. The formazan crystals were solubilized with 150 µL of DMSO, and absorbance was measured at 570 nm using a microplate reader. According to the MTT results, a concentration of 100 µg/mL was chosen for further cellular and molecular studies.

Live/dead (AO/PI) staining assay

To evaluate cytotoxicity, MC3T3-E1 cells underwent an AO/PI staining assay for days 1, 2, and 3. Cells were cultivated at a density of $2X10^4$ cells/well in 48 well plates and subjected to control, Ru, HA-HNT, and Ru2@HA-HNT at a concentration of 100 µg/mL for 24 hr. AO/PI staining was then employed to distinguish between viable and non-viable cells. A fluorescent microscope was used to view the stained cells after they had been incubated for 5 min [28].

Wound healing assay

An *in vitro* scratch wound healing experiment for days 1, 2 and 3 was performed to assess cell migration. Cells were cultivated at a density of $2X10^4$ cells per well in 48 well plates and subjected to control, Ru, HA-HNT, and Ru2@HA-HNT at a concentration of 100 µg/mL for 0, 12, and 24 hr. A uniform incision was created on the cell monolayer, and the migration of cells into the wounded area was monitored and documented at consistent intervals during a 24 hr. period (0, 12, and 24 h). This technique facilitates the observation of cellular mobility essential for tissue repair and regeneration.

DAPI staining

Cells were cultivated at a density of 2×10^4 cells per well in 48-well plates and subjected to Control, Rutin, HA-HNT, and Ru2@HA-HNT at a concentration of 100 µg/mL. DAPI was conducted on days 1, 2, and 3 by adding 100 µL of 4% paraformaldehyde to each well, which was incubated for 1 hr. The wells were subsequently rinsed with PBS solution, followed by the addition of 100 µL of 0.1% Triton X-100 to each

well and incubating for 10-15 minutes. Afterward, DAPI solution (300 nM), previously diluted at a ratio of 1:1000 with PBS solution, was added to each well and incubated for 15 minutes. The wells were subsequently rinsed with the PBS solution, and 100 µL of this solution was administered to each well and captured using a fluorescent microscope.

ROS detection and MMP

Cells were cultivated at a density of $2X10^4$ cells per well and subjected to control, Ru, HA-HNT, and Ru2@HA-HNT at a concentration of 100 µg/mL. Intracellular ROS were quantified for days 1, 2, and 3 with the DCFH-DA fluorescent probe. Following the seeding and treatment of MC3T3-E1 cells in 48 well plates for 24 hours, the cells were subsequently treated with DCFH-DA. The resultant fluorescence was subsequently examined with an inverted fluorescence microscope to qualitatively evaluate ROS generation. For the quantitative study, cells were collected, incubated with the probe, and their fluorescence was quantified using a fluorescent reader at an excitation wavelength of 488 nm and an emission wavelength of 525 nm.

MMP was evaluated for days 1, 2, and 3 with the fluorescent dye Rhodamine 123 (Rh123). MC3T3-E1 cells were inoculated at a density of 2×10^4 cells per well in 48-well plates and co-cultured with the experimental substances for 24 hr. Subsequent to the treatment time, the cells were rinsed with PBS and then stained with Rhodamine 123 (Rh123) for 20 min in darkness at 37°C. The Rh123 dye accumulates in the mitochondria in direct proportion to the MMP. Following a final wash to eliminate surplus dye, fluorescence pictures were obtained using an inverted fluorescence microscope to subjectively assess alterations in MMP.

Antibacterial assay

The antibacterial activity of the nanocomposites was evaluated against *S. aureus*, with Vancomycin (30 µg/mL) serving as the positive control. After agar solidification, the bacterial solution was homogeneously spread onto nutrient agar plates. Inoculated agar was coated with sterile filter paper discs saturated in 30 µg/mL test solutions. Plates were incubated at 37°C for 24 hr. AO and PI stains assessed bacterial viability following incubation. Bacterial cells were stained with the AO/PI solution and mounted on glass slides. The slides were then examined using a fluorescence microscope.

Alkaline Phosphatase (ALP) activity

ALP is an osteogenic marker whose activation is increased during bone formation; its expression increases at the onset of mesenchymal stem cell (MSC) differentiation. The increase in ALP expression promotes bone formation by nucleating calcium phosphate on the extracellular matrix, leading to mineralization and playing a crucial role in osteoblast differentiation and maturation. Cells were cultivated at a density of 2×10^4 cells per well in 48-well plates, and activities seen in control, HA-HNT, and Ru2@HA-HNT composite were administered to MC3T3-E1 pre-osteoblast cell line for durations of 1, 7, and 14 days to evaluate their ALP activities. Following incubation, the MC3T3-E1 pre-osteoblast cells were rinsed with PBS, lysed using lysis buffer, incubated for 30 min at 37°C, and subsequently stored for 12 hr at 4°C. The cells were subsequently centrifuged for 10 min at 12,000 rpm. The supernatant was combined with p-nitrophenyl phosphate solution (1:20) and incubated for 1 hr at 25°C. The ALP activity was assessed using the fluorescent microscopy equipment (Olympus, CKX53) at a wavelength of 405 nm.

Alizarin red dye (ARS) staining

ARS staining was employed to examine the bone differentiation. Cells were cultivated at a density of 2×10^4 cells per well in 48-well plates, and activities were seen in control, HA-HNT, Ru2@HA-HNT samples. The samples were stained on days 1, 7 and 14. Briefly, the cells were washed twice with PBS, fixed with10% formaldehyde for 30 min, and rinsed again with PBS. Following fixation, the cells were incubated with 1% alizarin red S solution for 10 to 15 min at pH 7.2 at RT. Residual stain was removed by thorough washing with distilled water. The stained cells were then examined with a light microscope to determine their calcium accumulation.

Immunofluorescence

MC3T3-E1 cells were cultured at a density of 2×10^4 cells per well in 48-well plates on control plates, pure Ru, HA-HNT, and Ru2@HA-HNT nanocomposites for 1, 2, and 3 days. At each time point, cells were fixed with 4 % paraformaldehyde in PBS for 15 min, followed by permeabilization with 0.1% Triton X-100 for 10 min. Non-specific binding was blocked with 1% bovine serum albumin (BSA) for 30 min. The cells were then incubated with primary antibodies against RUNX2, ALP, COL I, and OCN (diluted in 1% BSA) overnight at 4°C. After washing three times with PBS, the cells were incubated with Alexa Fluor-conjugated secondary antibodies for 1 hr at RT in the dark. Nuclei were counterstained with DAPI (4',6-diamidino-2-phenylindole) for 5 min. The samples were mounted with an anti-fade mounting medium, and images were captured using a fluorescence microscope.

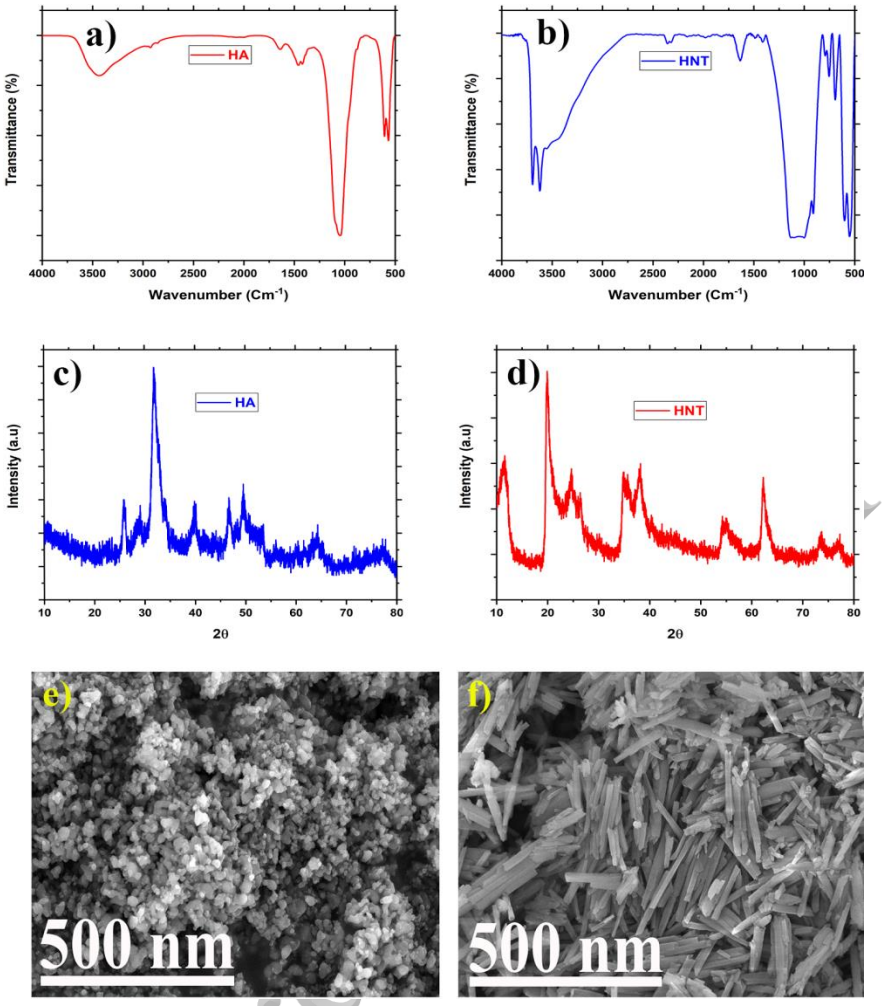

Fig. 1. FT-IR spectra of HA (a), and HNT nanotbular clay (b). XRD studies of HA (c), HNT (d). SEM images of HA (e), HNT nanotubes (f).

RESULT AND DISCUSSION

Characterization of HA, HNT starting materials

The structural integrity, phase purity, and morphology of the starting materials, HA and HNT, were methodically studied (Fig. 1). The FT-IR spectra of HA validated its chemical identification, exhibiting recognizable absorption bands for a hydroxyl group (–OH) at 3620 cm^{-1} and notable phosphate (PO_4^{3-}) vibrations at 1050 cm^{-1}(Fig. 1a). The HNT spectrum was distinctive, characterized by Si–O and Si–O–Si stretching vibrations in the range of 1000–1100 cm^{-1} and a notable Al–OH bending vibration at 910 cm^{-1}, aligning with its aluminosilicate composition (Fig. 1b). XRD examination confirmed the crystallinity and purity of both materials (Fig. 1c and d). The HA diffractogram had peaks that correspond precisely with the JCPDS- 09-0432 standard for human bone apatite, and the HNT pattern fully conformed to its designated JCPDS- 00-29-1487. Significantly, no peaks indicative of contaminants was seen in any sample. SEM imaging showed the different nano-morphologies (Fig. 1e and f). The HA material included homogeneous spherical nanoparticles with sizes ranging from 50 to 100 nm. Conversely, HNT exhibited its distinctive high-aspect-ratio tubular architecture, with diameters ranging from 50 to 100 nm, consistent with prior studies (Fig. 1f) [29].

Characterization of HA-HNT and Ru2@HA-HNT nanocomposite

The HA-HNT composite exhibited the typical peaks of O–H stretching at approximately 3620 cm^{-1}, asymmetric stretching, symmetric and bending vibrations of phosphate groups (PO_4^{3-}) at 1010cm^{-1}, 910 cm^{-1}, and 550 cm^{-1} [30]. A characteristic peak of HNT was observed at 910 cm^{-1}, which corresponds to the Al-OH bending vibration (Fig. 2a)[31]. The Ru2@HA-HNT spectra displayed the characteristic bands for HA-HNT matrix, confirming successful Ru loading without disrupting the composite's structure. Particularly, composites exhibited characteristic peaks at 3400 cm^{-1}, which corresponded to O–H stretching vibrations; 1650 cm^{-1} for C=O stretching; 1550 cm^{-1} for C=C vibrations in aromatic rings; 1360 cm^{-1} for C–O phenolic groups; and 1200 cm^{-1} for C-O-C stretching

vibrations, which were consistent with the spectral characteristics of Ru [32,33]. This finding suggests that the HA-HNT matrix and Ru molecules have strong interactions through hydrogen bonding between the hydroxyl groups of Ru and the phosphate or hydroxyl groups of the HA-HNT and surface adsorption. The XRD pattern of the HA-HNT and Ru2@HA-HNT composite exhibits distinctive diffraction peaks (Fig. 2b). A distinct crystalline HA phase will be characterized by its prominent and strong diffraction peaks. The principal peaks for stoichiometric HA, a hexagonal crystal structure, show at 2θ values of about 31.7°, 32.9°, and 25.9° corresponding to the (211), (300), and (002) planes, respectively, in accordance with standard JCPDS data (No. 09-0432). HNT displays distinct peaks at approximately 12.1° (001), 20° (011), and 24.1° (002), according to the basal spacing of the aluminosilicate layers. The mean nano-crystalline dimension (D) of the HA particles present in nanocomposites was determined utilizing the Scherrer equation:

$$D = 0.94\lambda/\beta\cos\theta \qquad (1)$$

where λ denotes the X-ray wavelength (1.5406 Å), β signifies the full width at half maximum (FWHM) of the diffraction peak in radians, and θ indicates the Bragg diffraction angle. The study of the principal reflection associated with the (211) plane revealed an average crystallite size of around 17.27 nm.

Moreover, XRD studies of the integration of Ru gradually modified the HA-HNT matrix. The Ru1@HA-HNT (1% Ru) preserved significant crystallinity; nonetheless, it likely constitutes a sub-therapeutic dosage that is safe yet perhaps insufficient to successfully prevent bacterial colonization or appropriately promote osteoblast development. In contrast, Ru3@HA-HNT (3% Ru) exhibited a marked decrease in peak intensity, suggesting that excessive Ru loading interfered with the structured development of HA crystals, resulting in amorphization. Consequently, Ru2@HA-HNT (2% Ru) was determined to be the optimum formulation. It maintains adequate crystallinity to guarantee the scaffold's structural integrity and resistance to swift degradation, while delivering a sufficiently high therapeutic dosage to effectively suppress bacterial proliferation, a crucial element in osteomyelitis management, without undermining the ceramic scaffold's lattice.

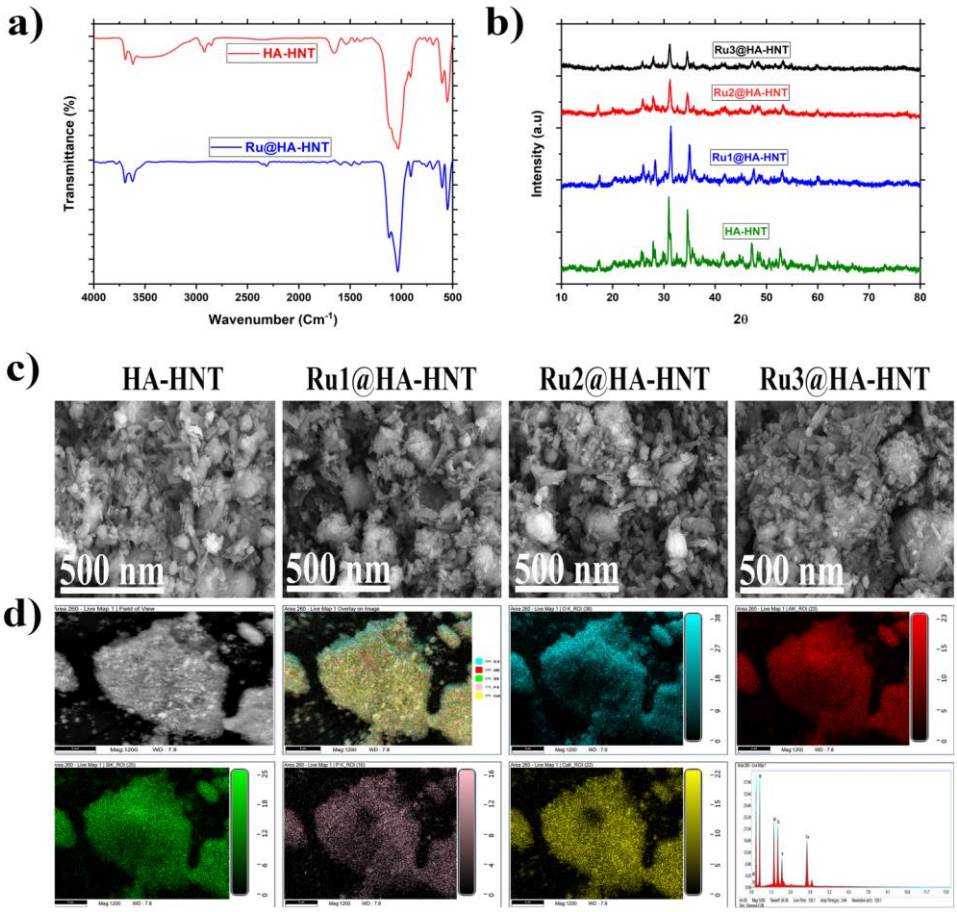

Fig. 2. FT-IR spectra of HA-HNT and Ru2@HA-HNT (a). XRD studies of HA-HNT and Ru1@HA-HNT, Ru2@HA-HNT, Ru3@HA-HNT (b). SEM images of HA-HNT, Ru1@HA-HNT, Ru2@HA-HNT, and Ru3@HA-HNT (c). Elemental mapping and EDAX analysis of HA-HNT nanocomposites (d).

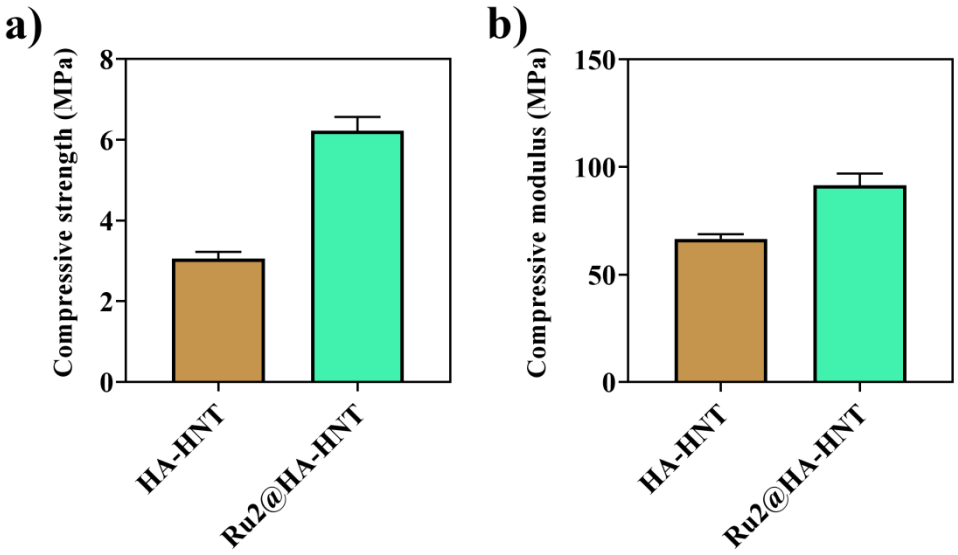

Fig. 3: Mechanical properties-compressive strength (a), compressive modulus (b) of HA-HNT, and Ru2@HA-HNT nanocomposites.

Morphological and Elemental Characterization

The surface morphology and elemental content of the produced nanocomposites were analyzed using SEM and EDAX respectively. Fig. 2c illustrates that the SEM micrographs of all formulations (HA-HNT, Ru1@HA-HNT, Ru2@HA-HNT, and Ru3@HA-HNT) validate a heterogeneous composite morphology. The photos clearly showed the existence of the two main inorganic constituents (HA-HNT): they have efficient interfacial contact and integration because HA nanoparticles are uniformly adhered to the HNT nanotube exterior surfaces. It has also been stated that a clear van der Waals force exists between nanoparticles and nanotubes [34,35]. A significant variation was seen according to the concentration of administered Ru. The Ru1@HA-HNT and Ru2@HA-HNT composites had a typically even particle distribution, but the high-concentration formulation (Ru3@HA-HNT) showed a propensity for larger nanoparticle size and agglomeration. This discovery, consistent with the XRD results, indicates that a high concentration of the bioactive ingredient may hinder the uniform creation of the nanocomposite, perhaps by disrupting nanoparticle nucleation and growth. Elemental mapping was conducted on the chosen Ru2@HA-HNT composite to verify the chemical composition and satisfactory integration of all components (Fig. 2d). The resultant elemental mapping and associated EDAX spectra clearly demonstrated the uniform distribution of Ca and P (HA), Al and Si (HNT), and C and O (Ru molecule). The co-localization of these components validates the effective synthesis of the hybrid nanocomposite. The XRD, SEM, and EDAX data together demonstrate that the Ru2@HA-HNT nanocomposite exhibits the most advantageous and uniform morphology, validating its choice for further biological studies.

Mechanical properties studies

The mechanical properties of the scaffolds were assessed to ascertain their appropriateness for load-bearing roles in bone tissue engineering. The HA-HNT scaffold demonstrated a compressive strength of 3.2 ± 1.12 MPa and a compressive modulus of 68 ± 0.85 MPa. The integration of Ru substantially improved the mechanical properties, resulting in the Ru@HA-HNT composite attaining a compressive strength of 6.2 ± 0.23 MPa and a modulus of 94 ± 0.71 MPa (Fig 3). The enhancement in compressive strength indicates that Ru molecules may function as interfacial coupling agents, establishing hydrogen bonds with the hydroxyl groups of the HA-HNT matrix, thus enhancing the density of particles and diminishing micro-porosity. The mechanical parameters of the Ru2@HA-HNT composite are significantly aligned with the typical ranges for human cancellous bone, specifically 2–12 MPa for strength and 10–2000 MPa for modulus [36]. This anatomical concordance verifies that the Ru2@HA-HNT scaffold has adequate mechanical integrity to facilitate cellular proliferation and endure physiological stresses at the implant site without mechanical failure.

Evaluation of cytocompatibility of Ru2@HA-HNT nanocomposites

The cytocompatibility of control, Ru, HA-HNT, and Ru2@HA-HNT nanocomposites was assessed *in vitro* using the MC3T3-E1 pre-osteoblast cell line, a recognized model for bone regeneration studies

pertinent to osteomyelitis therapy. The MTT experiment indicated that all evaluated control, Ru, HA-HNT, and Ru2@HA-HNT composites had favorable cell viability at doses between 10 and 100 µg/mL throughout a 24-hr period (Fig. 4a). The Ru2@HA-HNT nanocomposite exhibited elevated cell viability at all evaluated concentrations compared to the Ru, and HA-HNT groups. The findings indicated a dose-dependent enhancement in cell viability, with maximum viability recorded at 100 µg/mL. This observation is noteworthy, as it indicates that the integrated system is non-toxic and promotes cell proliferation, which maybe attributable to the advantageous properties of Ru and the biocompatibility of the HA-HNT matrix.

Microscopic images demonstrated the healthy morphology and proliferative activity of MC3T3-E1 cells cultured with control, Ru, HA-HNT, and Ru2@HA-HNT composite throughout 1, 2, and 3 days, with no detectable cytotoxicity (Fig. 4b). The control exhibited healthy cells, with spread cells proliferating throughout three days. The Ru2@HA-HNT nanocomposite demonstrated a strong and well-adhered morphology in comparison to the Ru, and HA-HNT composite. During days 1, 2, and 3, a significant rise in cell density was noted, suggesting that the cells were not just surviving but also proliferating. The microscopic images verify that the nanocomposites do not elicit any observable indicators of cytotoxicity, including cell shrinkage or detachment. The MTT assay and cell imaging investigations show that Ru2@HA-HNT scaffolds have superior cytocompatibility, making them a promising osteomyelitis therapy and aid in bone tissue regeneration.

Live/dead staining of MC3T3-E1 cells on Ru2@HA-HNT nanocomposites

Fig. 5 illustrates the live/dead staining of MC3T3-E1 cells subjected to control, Ru, HA-HNT, and Ru2@HA-HNT nanocomposites over 1, 2, and 3 days with AO/PI staining. The green area represents the nuclei of living cells stained with AO reagent, whereas the red region denotes the nuclei of dead cells labeled with PI reagent. On day 3, all groups displayed primarily green fluorescent cells with minimal red cells, signifying elevated cell viability across the treated groups. The Ru2@HA-HNT nanocomposites exhibited superior ability to promote cell proliferation and minimize the mortality rate of cells in comparison to Ru and HA-HNT composites over 1 to 3 days, indicating higher cytocompatibility and improved cell viability. The results validate that Ru2@HA-HNT promotes osteoblast viability, aligning with its potential for osteomyelitis treatment by integrating bioactive material for bone regeneration scaffolding.

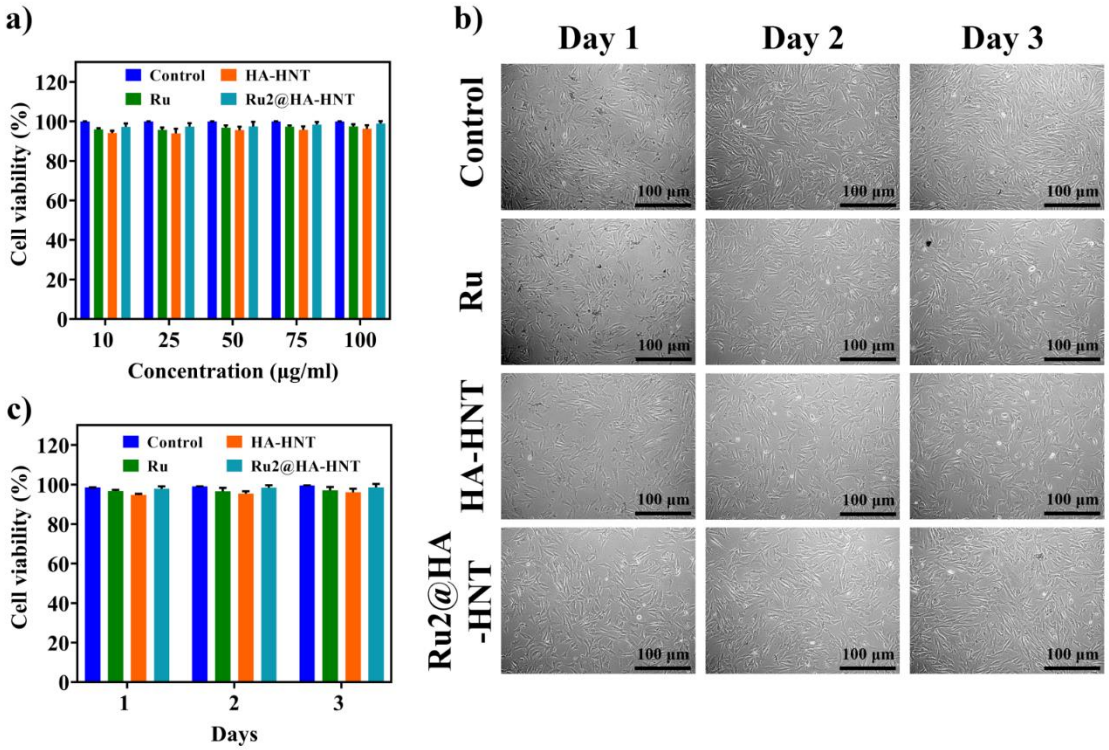

Fig. 4. Relative cell viability of MC3T3-E1 cells cultured with increasing concentrations (10-100 µg/mL) of Ru, HA-HNT, and Ru2@HA-HNT nanocomposites after 24 hours, accessed *via* an MTT assay (a). Cell proliferation assay demonstrating the viability of MC3T3-E1 cells cultured on Rutin, HA-HNT, and Ru2@HA-HNT nanocomposites over a 1, 2, and 3 days (b). Cell viability in percentage (%) (c).

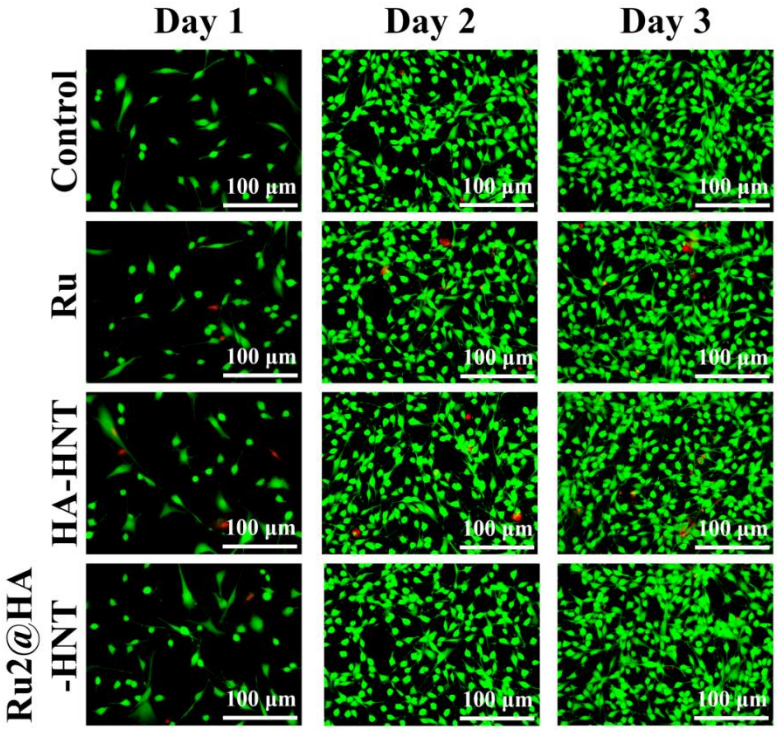

Fig. 5. Fluorescent micrographs depicting the viability of MC3T3-E1 cells cultured on Ru, HA-HNT, and Ru2@HA-HNT nanocomposites after 1, 2, and 3 days.

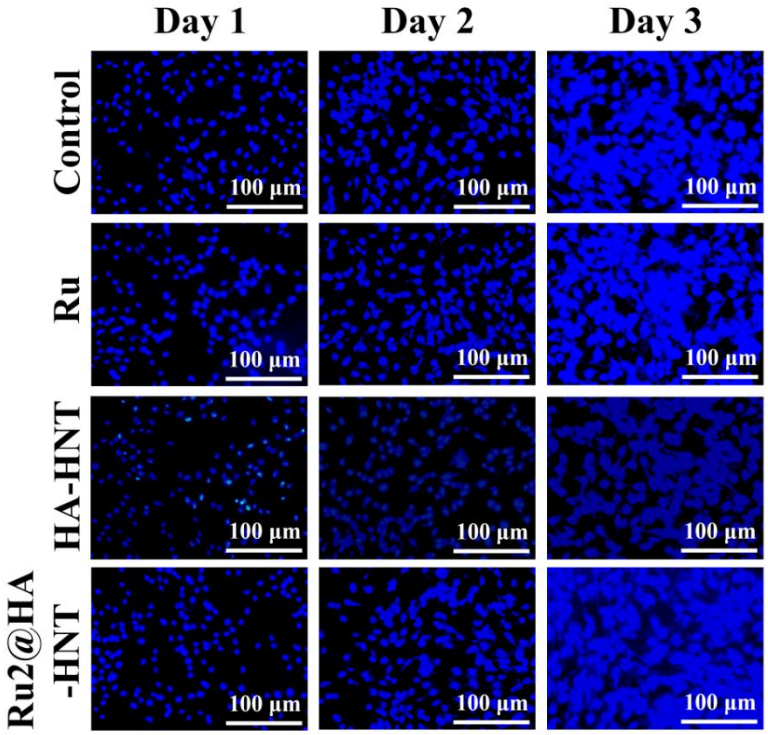

Fig. 6. DAPI-stained fluorescence micrographs of MC3T3-E1 cells showing cell nuclei (blue). The images show the density and morphology of cells cultivated on different treated groups at 1, 2, and 3 days.

DAPI staining

Fig. 6 illustrates DAPI stained pictures of MC3T3-E1 cells subjected to control, Ru, HA-HNT, and Ru2@HA-HNT nanocomposites during 1, 2, and 3 days. DAPI specifically attaches to DNA, producing intense blue fluorescence that accentuates cell nuclei [37]. On day 3, all groups had fluorescent nuclei, with the Ru2@HA-HNT group demonstrating

the most luminous and strong blue spots, signifying superior cell growth and nuclear integrity relative to the Ru and HA-HNT groups. In DAPI experiments, the HA-HNT composite demonstrated a slight reduction in blue fluorescence, suggesting a reduction in cell density attributable to the composite's restricted surface properties or potential cytotoxicity, which may hinder cell attachment and spreading. Following the incorporation of Ru, the composite exhibited optimal cell viability, presumably due to the bioactive and antioxidant characteristics of Ru, which improve cytocompatibility and facilitate cellular development and proliferation on the material. The findings validate that Ru2@HA-HNT nanocomposites improve osteoblastic cell viability and proliferation, endorsing their application in osteomyelitis therapy due to their superior cytocompatibility and biological activity.

ROS and MMP studies

ROS and MMP tests offer an essential understanding of the biological mechanisms underlying biocompatibility and toxicity. ROS are highly reactive chemicals that, when excessively created, can induce oxidative stress, resulting in cellular damage and mortality. Conversely, MMP serves as a crucial marker of mitochondrial integrity and cellular vitality; a reduction in MMP denotes a decline in mitochondrial functionality and represents an initial signal of apoptosis [38,39].

ROS and MMP fluorescence pictures of MC3T3-E1 cells treated with control, Ru, HA-HNT, and Ru2@HA-HNT nanocomposites at 1, 2, and 3 days are exhibited in Fig. 7a &b. The Ru2@HA-HNT nanocomposites and the control group both showed a significant reduction in ROS production as compared to the cells treated with Ru and HA-HNT, indicating the nanocomposite's capacity to efficiently scavenge ROS and reduce oxidative stress (Fig. 7a)[40]. This is likely due to the antioxidant properties of Ru, which effectively mitigate the oxidative stress caused by the material.

MMP analysis demonstrated that the Ru2@HA-HNT preserved mitochondrial function and cellular health by maintaining a sustained mitochondrial membrane potential at 1, 2, and 3 days (Fig. 7b). An increase in fluorescence intensity indicates a greater MMP, signifying healthy, non-apoptotic cells with preserved mitochondrial function. The nanocomposites exhibited superior fluorescence intensity relative to control, Ru, and HA-HNT, indicating that the Ru3@HA-HNT scaffold more efficiently preserves mitochondrial integrity and enhances cellular viability over time. This augmented fluorescence indicates the composite capacity to preserve mitochondrial polarization, therefore averting early apoptosis and facilitating extended cell survival.The results demonstrate that nanocomposites effectively treat osteomyelitis by reducing oxidative stress and maintaining mitochondrial function, both of which are essential for enhancing osteoblast activity.

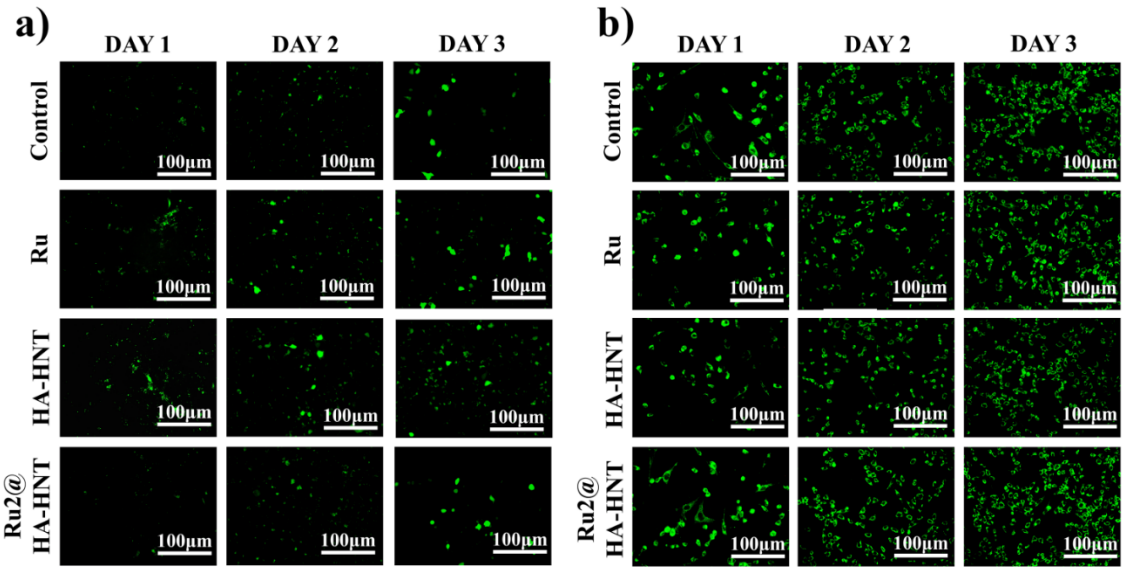

Fig. 7. Representative fluorescent pictures depicting intracellular ROS production (a), and MMP in MC3T3-E1 cells (b). Cells were grown with Ru, HA-HNT, and Ru2@HA-HNT nanocomposites at 1, 2, and 3 days.

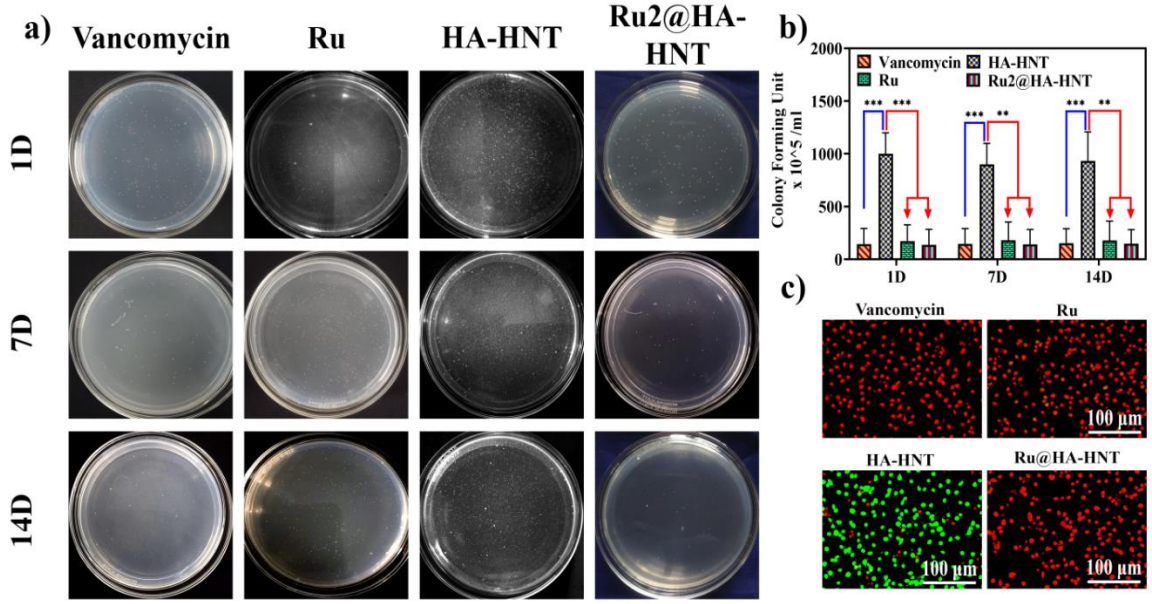

Fig. 8. Evaluation of the antibacterial properties of Vancomycin, Ru, HA-HNT, and Ru@HA-HNT nanocomposites against *S. aureus* over 1, 7, and 14 days. Representative photos depicting bacterial colony growth on nutrient agar plates (a). Quantitative assessment of colony-forming units (CFU), demonstrating bacterial viability rates (b). Fluorescence microscopy pictures obtained from the Live/Dead (AO/PI) experiment (c).

Antibacterial studies

The antibacterial efficiency and lethality of the Ru@HA-HNT nanocomposites against *S. aureus* were meticulously assessed over 1, 7, and 14 days using colony-forming unit (CFU) assays (Fig. 8a,b) and fluorescence-based Live/Dead labeling (Fig. 7c). As expected, the HA-HNT group exhibited negligible bactericidal activity (<10% killing efficiency), as indicated by dense colony formation and significant green fluorescence (AO uptake) signifying viable cells; however, the addition of Ru significantly improved the antibacterial efficacy. Pure Ru had considerable membrane-damaging properties, attaining an 89.5% lethality rate marked by a substantial proportion of red-fluorescing (PI-positive) non-viable cells. The Ru2@HA-HNT nanocomposite significantly maintained and improved this bioactivity, exhibiting a sustained lethal efficiency of 92.4% across the 14-day evaluation, closely approaching the 98.5% efficacy of the positive control. This consistent performance verifies that Ru@HA-HNT behaves as a durable bioactive material, providing a strong antibacterial option similar to traditional synthetic medicines.

Wound healing assay

A Wound healing assay was performed with MC3T3-E1 cells to evaluate cellular migration, a vital step in osteomyelitis therapy. The experiment was conducted using pure Ru, HA-HNT, and Ru2@HA-HNT treatments at 0, 12, and 24 hours (Fig. 9). A noticeable scratch was induced in the cell monolayer, and cell migration into the gap was observed and quantified over time. The progressive closure of scratches signifies enhanced migration, essential for osteogenesis and bone healing. Cells treated with Ru2@HA-HNT exhibited markedly improved migration relative to the control, with the most pronounced effect noted at an elevated dosage (100 µg/mL). Conversely, pure Ru and HA-HNT treatments yielded reduced migration rates compared to Ru2@HA-HNT, enabling the assessment of the flavonoid's inherent pro-migratory properties and the scaffold's influence, respectively. This assay illustrates the capacity of nanocomposites to enhance precursor osteoblast migration and facilitate bone healing in the contexts of osteomyelitis.

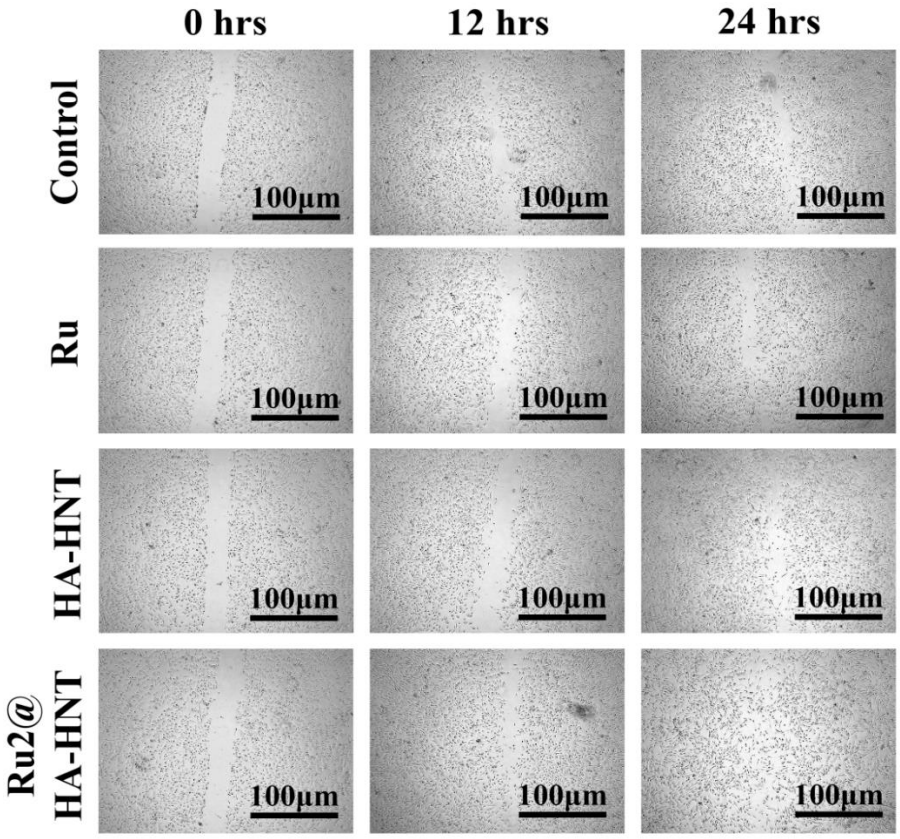

Fig. 9. A scratch assay on MC3T3-E1 cells assessing the pro-migratory effects of pure Ru, HA-HNT, and Ru2@HA-HNT nanocomposites at 0, 12, and 24 hrs.

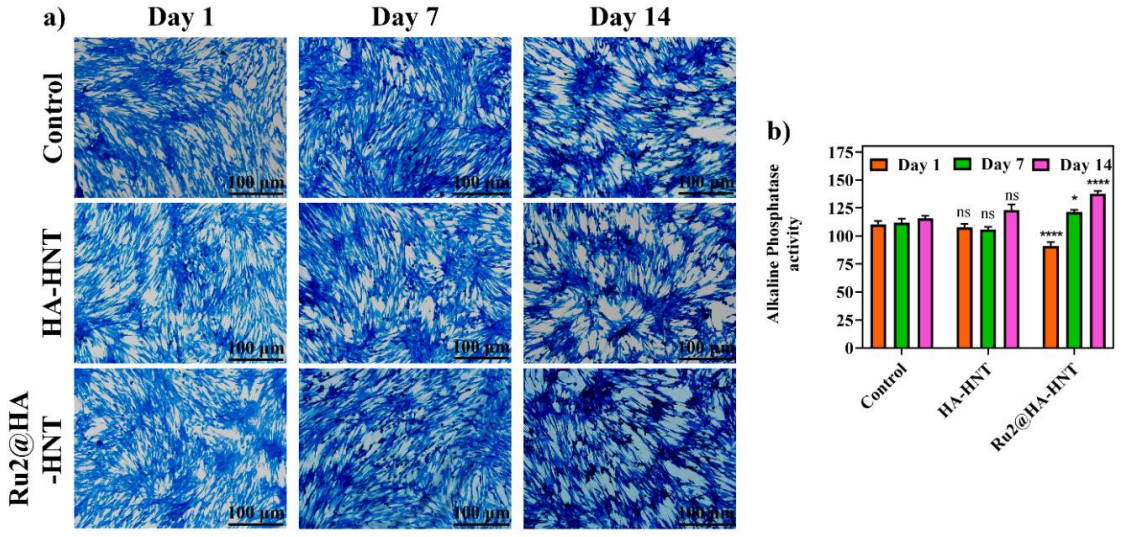

Fig. 10. Activity of alkaline phosphatase in MC3T3-E1 cells cultivated treated groups at 1, 7 and 14 days (a). Fold change in ALP activity (b).

Ru2@HA-HNT nanocomposites enhance the osteogenic differentiation in MC3T3-E1 Cells

The activity of ALP, a crucial indicator of osteoblastic development and extracellular matrix maturation, was significantly elevated by the Ru2@HA-HNT nanocomposites (Fig. 10). The quantitative evaluation, standardized to the control (100%), demonstrated a clear temporal advancement in osteogenic activity. In the initial phase (Day 1), both groups demonstrated a temporary decline in activity, with the HA-HNT and Ru2@HA-HNT groups reducing by 3% and 18%,

respectively, presumably due to initial cellular adaptation. By Day 7, a distinct alteration in bioactivity was noted: the HA-HNT group was 6% below the control, but the Ru2@HA-HNT group exhibited a recovery and improvement, reflecting an 8% increase compared to the control. By Day 14, this tendency escalated, with the Ru2@HA-HNT nanocomposites exhibiting a 19% enhancement in ALP activity relative to the control, markedly surpassing the HA-HNT group, which demonstrated only a 7% increase. The quantitative results were validated by ALP staining images, which revealed that the Ru2@HA-HNT group had a greater density of dark blue precipitates, signifying strong early-stage differentiation. This improved osteogenesis is mechanistically ascribed to the synergistic effects of the composite constituents: silicon released from HNT is recognized for its ability to stimulate Collagen I (COL I) secretion [41], while Ru and HA enhance osteogenic signaling pathways [42]. The results collectively demonstrate that the Ru2@HA-HNT nanocomposite substantially enhances ALP activity, establishing it as a viable bioactive scaffold for bone regeneration.

The calcium mineralization of MC3T3-E1 cells, an essential indicator of late-stage osteogenic differentiation, was evaluated using ARS staining over a culture duration of 1, 7, and 14 days (Fig. 11). Quantitative analysis standardized to the control (100%) demonstrated unique mineralization profiles for each group. During the initial phase (Day 1), mineral deposition was predominantly minimal; however, the Ru2@HA-HNT group exhibited a marginal benefit with a 3% enhancement in mineralization compared to the control, while the HA-HNT had a 12% decline. By Day 7, the difference became increasingly noticeable: the HA-HNT group was 10% below the control, but the Ru2@HA-HNT group demonstrated a consistent 8% increase, characterized by more intense and widespread red staining indicative of extracellular matrix mineralization initiation. On Day 14, the Ru2@HA-HNT nanocomposites exhibited the most significant calcium nodule development, attaining a 16% increase in mineralization relative to the control, while the HA-HNT group was 8% lower than the control group. The results validate that the Ru2@HA-HNT nanocomposite not only facilitates but also enhances the maturation of osteoblasts and the creation of a mineralized matrix, underscoring its exceptional bioactive potential for bone regeneration therapies [43].

Immunofluorescence staining

Immunofluorescence labeling was employed to elucidate the expression of critical osteogenic proteins RUNX2, ALP, COL I, and OCN in MC3T3-E1 cells (Fig. 12). Qualitative analysis demonstrated a clear hierarchy in protein expression: the HA-HNT and pure Ru groups exhibited moderate expression, whereas cells cultured on Ru2@HA-HNT nanocomposites displayed significantly elevated fluorescence intensity across all four markers, signifying enhanced osteogenic induction [44-48]. RUNX2, the principal transcription factor for osteogenesis, exhibited pronounced nuclear localization in the Ru2@HA-HNT group, indicating a strong dedication to the osteogenic lineage. This was accompanied by a significant rise in ALP fluorescence intensity, validating expedited early-stage differentiation and the beginning of matrix mineralization.

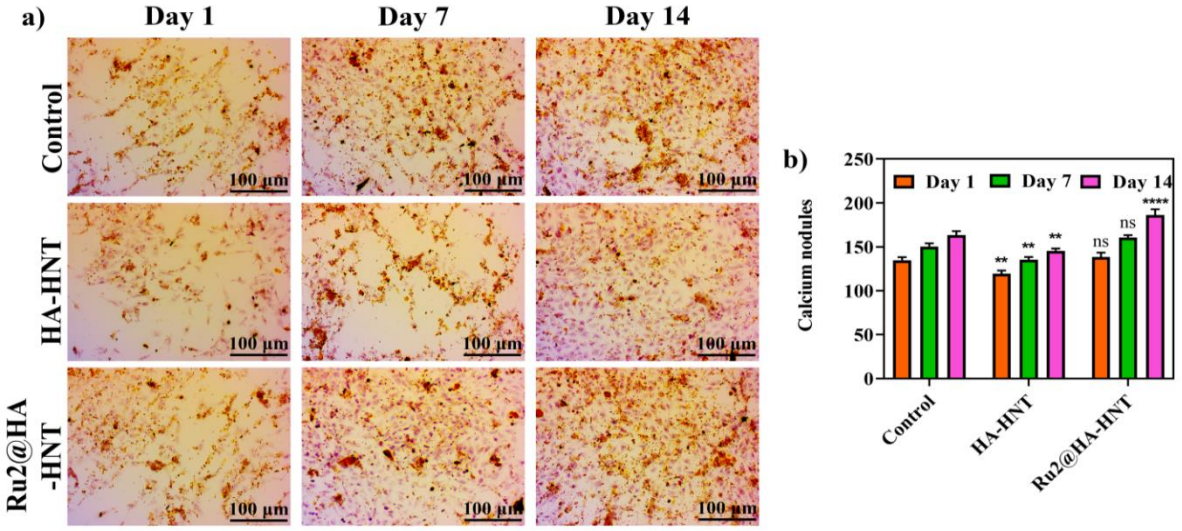

Fig. 11. Alizarin Red staining (ARS) in MC3T3-E1 cells cultivated on treated at different time intervals (1, 7, and 14 days). Fold change in calcium nodules (b).

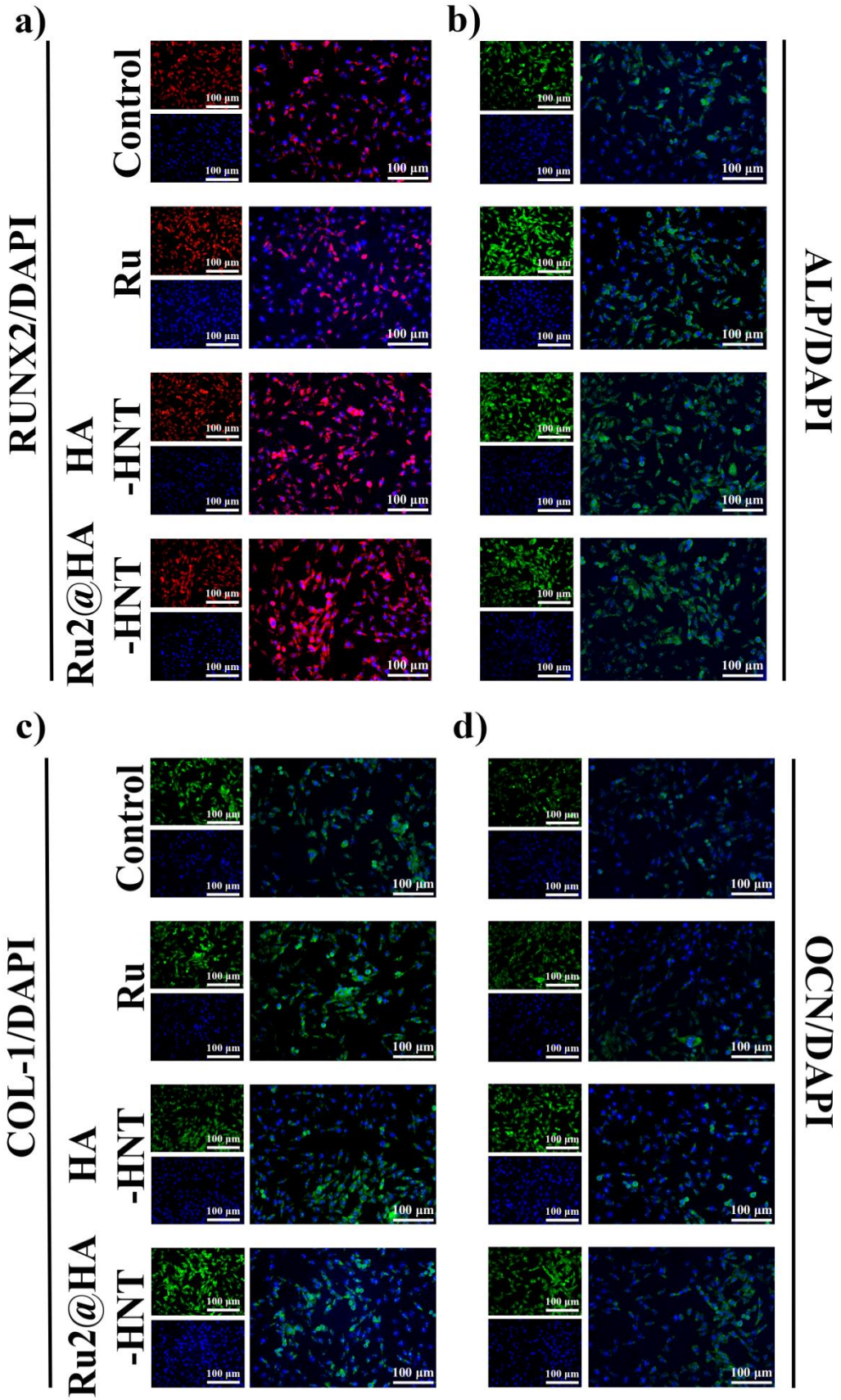

Fig. 12. Immunofluorescence of osteogenic-related proteins expression RUNX2 (a), ALP (b), COL I (c), and OCN (d) in MC3T3-E1 cells cultured on control, pure Ru, HA-HNT, and Ru2@HA-HNT nanocomposites.

The extracellular matrix of the Ru2@HA-HNT group exhibited dense, bright staining for Type I Collagen (COL I), signifying increased protein synthesis and the development of a robust structural framework crucial for new bone formation. In the advanced stages of maturation, the elevated expression of Osteocalcin (OCN) is substantially greater than in control groups, validating that the nanocomposite effectively facilitates the concluding phases of osteoblast development. This extensive upregulation is likely due to Ru, whose intrinsic antioxidant and anti-inflammatory characteristics foster an ideal milieu for osteogenic signaling. The results collectively indicate that Ru2@HA-HNT nanocomposites markedly enhance the synthesis and maturation of critical bone proteins, confirming their promise for efficient bone tissue regeneration.

CONCLUSIONS

This study effectively synthesized and assessed a multifunctional Ru@HA-HNT nanocomposite, confirming its dual effectiveness in treating osteomyelitis and facilitating bone regeneration. A physicochemical study verified the steady incorporation of Ru into the HA-HNT matrix by hydrogen bonding. The integration of HNT enhanced the scaffold, achieving a compressive strength similar to cancellous bone, thereby guaranteeing the necessary structural integrity for load-bearing applications. The nanocomposite exhibited a synergistic therapeutic effect by demonstrating significant antibacterial activity against *S. aureus* while simultaneously scavenging ROS to alleviate oxidative stress. This bioactive milieu markedly improved the proliferation and differentiation of MC3T3-E1 pre-osteoblasts, as seen by elevated calcium mineralization and the upregulation of essential osteogenic markers (RUNX2, ALP, COL I, and OCN). Although these encouraging results, particular limitations of the present investigation must be recognized to inform future applications. While intrinsic biocompatibility and mechanical competency were confirmed, long-term systemic toxicity and biodegradation profiles were not assessed. Moreover, the translation of these *in vitro* findings requires validation through *in vivo* animal models to confirm osseointegration and bacterial elimination within a complicated physiological context. Thus, subsequent research will concentrate on *in vivo* preclinical trials to comprehensively confirm the clinical safety and effectiveness of this bioactive system for dual-purpose osteomyelitis treatment.

ACKNOWLEDGEMENT

There is no acknowledgement in this work

CONFLICTS OF INTEREST

I assert that the authors possess no conflicting interests.

FUNDING

The authors did not receive any financial assistance for the research, authorship, or publishing of this work.

ETHICAL CONSIDERATION

This study encompassed solely *in vitro* analysis. This study did not involve any human participants or animal subjects, including rats, mice, or rabbits. Consequently, ethical approval and informed consent were unnecessary.

AI STATEMENT

The authors assert that no artificial intelligence (AI) tools were employed in the design, analysis, or production of this publication.

AUTHORS CONTRIBUTIONS

P.J – Conceptualization, data curation, methodology, validation, visualization, writing – original draft, software, writing – review and editing; **M.B** – Conceptualization, data curation, validation, visualization, writing – original draft, writing – review and editing; **P.R.B** – Conceptualization, data curation, formal analysis, funding acquisition, investigation, methodology, supervision, validation, writing – original draft, writing – review and editing.

DATA ACCESSIBILITY

The datasets produced in this study can be obtained from the corresponding author upon reasonable request.

REFERENCES

1. Urish KL, Cassat JE. Staphylococcus aureus osteomyelitis: bone, bugs, and surgery. Infect Immun. 2020; 88(7).
2. Wu S, Wu B, Liu Y, Deng S, Lei L, Zhang H. Mini review therapeutic strategies targeting for biofilm and bone infections. Front Microbiol. 2022; 13.
3. Hofstee MI, Muthukrishnan G, Atkins GJ, Nizet V, Bonhoeffer S, Zinkernagel AS, et al. Current concepts of osteomyelitis. Am J Pathol. 2020; 190(6): 1151–1163.
4. Mouzopoulos G, Kanakaris NK, Kontakis G, Obakponovwe O, Townsend R, Giannoudis PV. Management of bone infections in adults: the surgeon's and microbiologist's perspectives. Injury. 2011; 42(Suppl 5): S18–S23.

5. Masters EA, Ricciardi BF, Bentley KL de M, Moriarty TF, Schwarz EM, Muthukrishnan G. Skeletal infections: microbial pathogenesis, immunity and clinical management. Nat Rev Microbiol. 2022; 20.
6. Zapata D, Higgs J, Wittholt H, Chittimalli K, Brooks AE, Mulinti P. Nanotechnology in the diagnosis and treatment of osteomyelitis. Pharmaceutics. 2022; 14(8): 1563.
7. Stobba BK, Kasprzak M. Fabrication of nanoparticles for bone regeneration: new insight into applications of nanoemulsion technology. J Mater Chem B. 2021; 9: 5221–5244.
8. Ielo I, Calabrese G, De Luca G, Conoci S. Recent advances in hydroxyapatite-based biocomposites for bone tissue regeneration in orthopedics. Int J Mol Sci. 2022; 23(17): 9721.
9. Hatami Kaleshtari A, Farjaminejad S, Hasani M, Farjaminejad R, Gharibshahian M, Zafari M, et al. The critical role of nano-hydroxyapatites as an advanced scaffold in drug delivery towards efficient bone regeneration: recent progress and challenges. Carbohydr Polym Technol Appl. 2025; 9: 100692.
10. Jamarun N, Afriska LN, Wellia DV, Arief S, Aziz H, Ismail A, et al. Investigation of the antibacterial activity of synthesized hydroxyapatite Sr-doped nanocomposite. J Appl Pharm Sci. 2024; 14(9).
11. Kyeremeh SP, Asimeng BO, Paemka L, Kojo MA, Annan E, Tiburu EK. Antibacterial activity of microwave hydroxyapatite and cellulose blend. Oxf Open Mater Sci. 2024; 4(1): itae010.
12. Zhao C, Liu W, Zhu M, Wu C, Zhu Y. Bioceramic based scaffolds with antibacterial function for bone tissue engineering: a review. Bioact Mater. 2022; 18.
13. Yadav U, Verma V. Halloysite nanoclay reinforced hydroxyapatite porous scaffold for hard tissue regeneration. J Mech Behav Biomed Mater. 2023; 140: 105626.
14. Wang C, Guo T, Gong Y, Xu L, Zhang J, Chen Y, et al. Novel polydopamine/halloysite nanotube-reinforced brushite calcium phosphate cement for bone regeneration with synergistic regulation of mechanical/osteogenic capacity. Mater Adv. 2025; 6: 1959–1964.
15. Same S, Akbari Nakhjavani S, Samee G, Agbolaghi S, Jahanban-Esfahlan R, Omidi Y, et al. Halloysite clay nanotube in regenerative medicine for tissue and wound healing. Ceram Int. 2022; 48: 31065–31079.
16. Ahmad R, Singh A, Purba A, Rashidinejad A. Novel rutin casein composites as functional dry ingredients for the delivery of high concentration of rutin in dairy beverages: in vitro bioaccessibility, cytotoxicity, absorption, and intestinal barrier integrity. Food Hydrocoll. 2025; 170: 111735.
17. Akash SR, Tabassum A, Aditee LM, Rahman A, Hossain MI, Hannan MA, et al. Pharmacological insight of rutin as a potential candidate against peptic ulcer. Biomed Pharmacother. 2024; 177: 116961.
18. Singh A, Kundu M, Chatterjee S, Das S, Ghosh S, Chattopadhyay N, et al. Synthesis of rutin loaded nanomagnesia as a smart nanoformulation with significant antibacterial and antioxidant properties. Inorg Chem Commun. 2022; 140: 109492.
19. Ivanov M, Novović K, Malesevic M, Dinic M, Stojković D, Jovcic B, et al. Polyphenols as inhibitors of antibiotic resistant bacteria: mechanisms underlying rutin interference with bacterial virulence. Pharmaceuticals. 2022; 15(3): 385.
20. Esnaashari F, Zahmatkesh H. Antivirulence activities of rutin loaded chitosan nanoparticles against pathogenic Staphylococcus aureus. BMC Microbiol. 2024; 24(1).
21. Liu XW, Ma B, Zi Y, Xiang LB, Han TY. Effects of rutin on osteoblast MC3T3-E1 differentiation, ALP activity and Runx2 protein expression. Eur J Histochem. 2021; 65(1): 3195.
22. Hyun H, Park H, Jeong J, Kim J, Kim H, Oh HI, et al. Effects of watercress containing rutin and rutin alone on the proliferation and osteogenic differentiation of human osteoblast like MG-63 cells. Korean J Physiol Pharmacol. 2014; 18(4): 347.
23. Abdel-Naim AB, Alghamdi AA, Algandaby MM, Al-Abbasi FA, Al-Abd AM, Eid BG, et al. Rutin isolated from Chrozophora tinctoria enhances bone cell proliferation and ossification markers. Oxid Med Cell Longev. 2018; 2018: 5106469.
24. Vijayalekha A, Sridhar H, Srinivasan S, Anumaiya V, Anandasadagopan SK, Pandurangan AK. Integrative network pharmacology and experimental validation of rutin-infused collagen–hydroxyapatite scaffold for promoting osteochondral regeneration. 3 Biotech. 2025; 15(9): 290.
25. Dadgar A, Maleki Dizaj S, Alizadeh Oskoee P, Pournaghi-Azar F, Jafari Navimipour E. Gelatin nanofibrous scaffolds containing rutin nanoparticles: physicochemical properties, antibacterial action, and anti-inflammatory effect on dental pulp stem cells. BMC Oral Health. 2025; 25: 1129.
26. Kyriacou H, Kamaraj A, Khan WS. Developments in antibiotic-eluting scaffolds for the treatment of osteomyelitis. Appl Sci. 2020; 10: 2244.
27. Memar MY, Dalir Abdolahinia E, Yekani M, Kouhsoltani M, Sharifi S, Maleki Dizaj S, et al. Preparation of rutin-loaded mesoporous silica nanoparticles and evaluation of its physicochemical, anticancer, and antibacterial properties. Mol Biol Rep. 2022; 50: 203–213.
28. Hussain H, L SR, Ahmad S, Abd Razak MF, Wan Mustapha WA, Zainol MK, et al. Determination of cell viability using acridine orange/propidium iodide dual spectrofluorometry assay. Cogent Food Agric. 2019; 5(1): 1582398.
29. Kalaiyarasi J, Meenakshi S, Gopinath SCB, Pandian K. Mediator free simultaneous determination of acetaminophen and caffeine using a glassy carbon electrode modified with a nanotubular clay. Microchim Acta. 2017; 184: 4485–4494.
30. Manoj M, Mangalaraj D, Ponpandian N, Viswanathan C. Core–shell hydroxyapatite/Mg nanostructures: surfactant free facile synthesis, characterization and their in vitro cell viability studies against leukaemia cancer cells (K562). RSC Adv. 2015; 5: 48705–48711.
31. Barot T, Rawtani D, Kulkarni P. Physicochemical and biological assessment of silver nanoparticles immobilized halloysite nanotubes-based resin

composite for dental applications. Heliyon. 2020; 6(3): e03601.
32. Luo S, Fu Y, Ye J, Liu C. Encapsulation of rutin in protein nanoparticles by pH-driven method: impact of rutin solubility and mechanisms. J Sci Food Agric. 2024; 104(3): 1804–1812.
33. Li C, Chen L, McClements DJ, Peng X, Xu Z, Meng M, et al. Preparation and characterization of rutin-loaded zein–carboxymethyl starch nanoparticles. Foods. 2022; 11(18): 2827.
34. Khan S, Kumar V, Roy P, Kundu PP. TiO2 doped chitosan/hydroxyapatite/halloysite nanotube membranes with enhanced mechanical properties and osteoblast like cell response for application in bone tissue engineering. RSC Adv. 2019; 9(68): 39768–39779.
35. Rance GA, Marsh DH, Bourne SJ, Reade TJ, Khlobystov AN. van der Waals interactions between nanotubes and nanoparticles for controlled assembly of composite nanostructures. ACS Nano. 2010; 4(8): 4920–4928.
36. Zia I, Mirza S, Jolly R, Rehman S, Owais M, Shakir M. Trigonella foenum graecum seed polysaccharide coupled nano hydroxyapatite-chitosan: a ternary nanocomposite for bone tissue engineering. Int J Biol Macromol. 2018; 124: 88–101.
37. Zheng J, Wu F, Li H, Liu M. Preparation of bioactive hydroxyapatite@halloysite and its effect on MC3T3-E1 osteogenic differentiation of chitosan film. Mater Sci Eng C. 2019; 105: 110072.
38. Hong D, Chen HX, Yu HQ, Liang Y, Wang C, Lian QQ, et al. Morphological and proteomic analysis of early stage of osteoblast differentiation in osteoblastic progenitor cells. Exp Cell Res. 2010; 316(14): 2291–2300.
39. Hong Y, Boiti A, Vallone D, Foulkes NS. Reactive oxygen species signaling and oxidative stress: transcriptional regulation and evolution. Antioxidants. 2024; 13(3): 312.
40. Li N, Oquendo E, Capaldi RA, Robinson JP, He YD, Hamadeh HK, et al. A systematic assessment of mitochondrial function identified novel signatures for drug induced mitochondrial disruption in cells. Toxicol Sci. 2014; 142(1): 261–273.
41. Reffitt DM, Ogston N, Jugdaohsingh R, Cheung HFJ, Evans BAJ, Thompson RPH, et al. Orthosilicic acid stimulates collagen type I synthesis and osteoblastic differentiation in human osteoblast like cells in vitro. Bone. 2003; 32(2): 127–135.
42. Jin Y, Liu X, Liu H, Chen S, Gao C, Ge K, et al. Oxidative stress induced apoptosis of osteoblastic MC3T3-E1 cells by hydroxyapatite nanoparticles through lysosomal and mitochondrial pathways. RSC Adv. 2017; 7(21): 13010–13018.
43. Porter AE, Patel N, Skepper JN, Best SM, Bonfield W. Comparison of in vivo dissolution processes in hydroxyapatite and silicon substituted hydroxyapatite bioceramics. Biomaterials. 2003; 24(25): 4609–4620.
44. Li Q, Wu Y, Zhang Y, Mao J, Zhang Z. Enhancing osteogenic differentiation of MC3T3-E1 cells during inflammation using UPPE/β-TCP/TTC composites via the Wnt/β-catenin pathway. RSC Adv. 2024; 14(3): 1527–1537.
45. Wu Y, Wang Y, Chen F, Wang B. Loading rutin on surfaces by the layer-by-layer assembly technique to improve the oxidation resistance and osteogenesis of titanium implants in osteoporotic rats. Biomed Mater. 2024; 19(4): 045011.
46. Xiao S, Wang M, Wang L, Zhu Y. Environment friendly synthesis of trace element Zn, Sr, and F codoping hydroxyapatite with non cytotoxicity and improved osteoblast proliferation and differentiation. Biol Trace Elem Res. 2018; 185(1): 148–161.
47. Hu S, Meng Z, Zhou J, Wang W, Liu Y, Liu W, et al. Enhanced attachment and collagen type I deposition of MC3T3-E1 cells via electrohydrodynamic printed sub microscale fibrous architectures. Int J Bioprint. 2022; 8(2): 514.
48. Valdez-Salas B, Castillo-Uribe S, Beltran-Partida E, Curiel-Alvarez M, Perez-Landeros O, Guerra-Balcazar M, et al. Recovering osteoblast functionality on TiO2 nanotube surfaces under diabetic conditions. Int J Nanomedicine. 2022; 17: 5469–5488.